Mechanical excitation and marginal triggering during avalanches in sheared amorphous solids

Richard, D.; Elgailani, A.; Vandembroucq, D.; Manning, M.L.; Maloney, C.E.

DOI
10.1103/PHYSREVE.107.034902

Publication date
2023

Document Version
Final published version

Published in
Physical Review E - Statistical, Nonlinear, and Soft Matter Physics

Mechanical excitation and marginal triggering during avalanches in sheared amorphous solids

D. Richard,[1,2,3,*] A. Elgailani,[4,*] D. Vandembroucq,[5] M. L. Manning,[2] and C. E. Maloney[4]
[1]*Institute for Theoretical Physics, University of Amsterdam, Science Park 904, Amsterdam, Netherlands*
[2]*Department of Physics and BioInspired Institute, Syracuse University, Syracuse, New York 13244, USA*
[3]*Univiversité Grenoble Alpes, CNRS, LIPhy, 38000 Grenoble, France*
[4]*Northeastern University, Boston, Massachusetts 02115, USA*
[5]*PMMH, CNRS UMR 7636, ESPCI Paris, PSL University, Sorbonne Université, Université de Paris, F-75005 Paris, France*

(Received 4 March 2022; accepted 26 February 2023; published 15 March 2023)

We study plastic strain during individual avalanches in overdamped particle-scale molecular dynamics (MD) and mesoscale elastoplastic models (EPM) for amorphous solids sheared in the athermal quasistatic limit. We show that the spatial correlations in plastic activity exhibit a short length scale that grows as $t^{3/4}$ in MD and ballistically in EPM, which is generated by mechanical excitation of nearby sites not necessarily close to their stability thresholds, and a longer lengthscale that grows diffusively for both models and is associated with remote marginally stable sites. These similarities in spatial correlations explain why simple EPMs accurately capture the size distribution of avalanches observed in MD, though the temporal profiles and dynamical critical exponents are quite different.

DOI: 10.1103/PhysRevE.107.034902

I. INTRODUCTION

Many driven disordered solids, ranging from glasses to granular matter to magnetic systems, respond via complex avalanches that are difficult to predict [1–3]. A better understanding of these dynamics, even in simple model systems, would aid in avalanche detection and material design.

We focus here on amorphous solids subject to slowly imposed shear that fail via a broad spectrum of avalanches of plastic deformation caused by redistribution of stress after local yielding events [4–7]. The highly anisotropic and long-range nature of the stress redistribution leads to a characteristic structure of the avalanches, where correlations are strongest along the directions of maximum imposed shear. Most previous work has focused on the distribution of avalanche sizes [7–13] and the spatial correlations of plastic strain, which develops over the course of successive avalanches [14–18]. More recently, the dissipation rate as a function of time during individual avalanches was studied in experiments on bulk metallic glass (BMG) pillars [19] and in a computer model [11]. The temporal response was observed to be similar to that in previously explored dynamically critical systems [4] and explained using a mean-field theory [19]. However, surprisingly, no work, in either experiment or simulation has yet characterized how the individual avalanches proceed in time *and space*.

To address this question we turn to computational models, including particle-based simulations such as molecular dynamics (MD) and related energy minimization techniques, which have been the workhorse for modeling sheared amorphous solids for decades, as well as elastoplastic models (EPMs). EPMs assume an amorphous solid is composed of mesoscale regions that will yield when the local stress reaches a specified threshold. There are many different versions of EPMs [20] that differ in how they introduce disorder, evolve propagating stress fields, etc. In perhaps the simplest class of EPM [7,8,21–23], the system is evolved quasistatically and, after any instability, the stresses are fully equilibrated over all space—effectively instantaneously—before allowing for any subsequent yielding. This is in contrast to MD simulations where, after a local rearrangement, the stress change propagates continuously in time and space—diffusively for overdamped systems [24] and ballistically for underdamped systems—away from the plastic instability.

Despite the fact that the quasistatic EPMs are completely devoid of any realistic description of the dynamics of stress redistribution, they capture the critical scaling exponents observed in overdamped MD simulations [9,25,26]. They are therefore, in some sense, unreasonably good, and the reason for their fidelity demands an explanation.

As a first step to elucidate this issue, in this paper we propose to compare avalanche dynamics in two very different systems that, despite their differences, share the same *static* exponents: (i) a realistic particle based simulation (falling into the overdamped universality class) and (ii) a simple deterministic EPM, with instantaneous stress redistribution devoid of any realistic temporal stress redistribution or mechanical nonlinearities present in the particle model. We show that while the temporal profile of the avalanches is quite different in the two models—the EPM agrees with previously known mean-field results while the MD does not—the spatial structure of the correlations that develop is strikingly similar.

The spatial correlation functions of plastic strain *within* a single avalanche are anisotropic, with strong correlations along the directions of maximum stress, as previously seen

[*]These authors contributed equally to this work.

in the plastic strain *accumulated* over many successive avalanches [14,15,17]. The structure of the correlation function and its evolution in time is similar in both MD and EPM. During the course of a single avalanche, the correlation function remains strongest along the principal shear axes in a strip which does not widen appreciably in time but does lengthen. At any given time, the correlations along the strip initially decay with distance as $e^{-r/\xi_{\text{excite}}}$ and cross through zero at a finite distance, ξ_{marginal}. We show that ξ_{excite} grows ballistically in time for the EPM, and we argue that the reason for this ballistic propagation is the "mechanical excitation" mechanism suggested by Idema and Liu [27]: one event generates a stress redistribution that causes nearby sites to exceed their threshold for stability, triggering new events. If the timescale over which an unstable site transforms is short compared to the propagation of the stress, then the resulting dynamics are reminiscent of toppling dominos, with a ballistic wave speed equal to the spacing of the dominos divided by the "toppling time"—the time it takes one, once destabilized, to fall onto its neighbor. ξ_{excite} grows less quickly in time for the MD, but it is still strongly superdiffusive, suggesting that a similar mechanism is at play and hinting that the "toppling time" in MD is more complicated than in EPM. In contrast, ξ_{marginal} grows diffusively in time for both models, and it has a pronounced system-size dependence. At long distance the low positive and negative contributions of the quadrupolar stress interactions add up as a mechanical noise and are expected to drive local zones close to marginality [28–32]. The observed size dependence suggests that ξ_{marginal} is the length scale at which the weakest sites in the system are close enough to the triggering event to be destabilized.

II. METHODS

A. Atomistic simulations

Our MD glass former consists of a standard two-dimensional 50:50 binary mixture of "large" and "small" particles of equal mass interacting via a short-range, nonadditive potential [33]. Pairs of particles i, j at distance r_{ij} from each other interact via a modified inverse-power-law pairwise potential,

$$\varphi_{\text{IPL}}(r_{ij}) = \begin{cases} \varepsilon\left[\left(\frac{\sigma_{ij}}{r_{ij}}\right)^{\beta} + \sum_{l=0}^{q} c_{2l}\left(\frac{r_{ij}}{\sigma_{ij}}\right)^{2l}\right] & , \quad \frac{r_{ij}}{\sigma_{ij}} \leqslant x_c \\ 0 & , \quad \frac{r_{ij}}{\sigma_{ij}} > x_c \end{cases}, \tag{1}$$

where ε is a microscopic energy scale. Distances in this model are measured in terms of the interaction length scale σ between two "small" particles, and the rest are chosen to be $\sigma_{ij} = 1.18\sigma$ for one "small" and one "large" particle, and $\sigma_{ij} = 1.4\sigma$ for two "large" particles. The coefficients c_{2l} are determined by demanding that $\varphi_{\text{IPL}}(r_{ij})$ vanishes continuously up to q derivatives [33]. In order to create poorly annealed glasses without permanent localization, we minimize liquids that are equilibrated at a high temperature $T = 2$, much higher than the computer glass transition $T_g \simeq 0.5$. A detailed discussion on how the parent temperature of the equilibrium liquid affects the elastic heterogeneities and mechanical response of the system can be found in Refs. [34,35].

We have considered different system sizes $L = 80, 160, 320$, and 640, respectively, with number density $\rho = N/V = 0.86$. Glasses are athermal and quasistatically sheared (AQS) up to 50% of strain (with strain step $\Delta\gamma = 10^{-4}$), and data reported here correspond to strains ranging from 20% to 50%. Our protocol is a simple shear deformation along the x axis; see Supplemental Material (SM) [36] for typical stress-strain curves.

Variations in strain step are discussed in the SM. At the onset of each instability, we trigger the avalanche by affinely deforming the system and subsequently letting the system relax via gradient descent dynamics according to $\dot{\mathbf{r}} = -D\nabla U$, with coordinate positions $\mathbf{r}$ and potential energy U. During the minimization process, we monitor the plastic deformation (i.e., the incremental nonaffine displacement) in the standard way by computing the D^2_{min} field [37] between snapshots separated by $2\tau_{MD}$, where the microscopic time is defined as $\tau_{MD} = \sigma^2/D$, with σ a typical particle diameter and D the bare translational diffusion coefficient. We have collected 20k and 1.2k avalanche dynamics for the smallest ($L = 80$) and largest ($L = 640$) system, respectively. The avalanche size S is defined as the total energy drop. The beginning of the avalanche at t_{start} is defined when the energy dissipation rate $-dU/dt > 0.1$, and the end of the avalanche at t_{end} is located from the latest time at which $-dU/dt > 0.1$. From this procedure we compute the avalanche duration as $T = t_{\text{end}} - t_{\text{start}}$. This procedure, chosen for its simplicity, is similar to the one described in Ref. [32], which focused on the time needed to destabilize the first site and time to reach the final mechanically equilibrated state.

B. Persistent homology

In order to break up a large avalanche into a sequence of individual plastic events that can be compared with EPM, we are inspired by a recently proposed persistent homology method [38]. Throughout the paper we refer to the location of each individual event as a "site." During each avalanche we record the incremental D^2_{min} plastic field which generates a representation of the activity on a grid of space-time regions, see Fig. 1(a). The spatial grid size is set to two particle diameters and the temporal grid size to 2 MD time units. The D^2_{min} of a cell corresponds to the sum over all D^2_{min} particle values within the cell. Our goal is to agnostically break up high local maxima of this space-time field. Here we first sort all D^2_{min} values from the largest to the lowest up to 10^{-3} (below which no actual plastic rearrangements occur). We then prune this sorted list and create a new cluster for each local maximum that does not belong to an existing cluster, where the clustering distance criterion is set to the first neighbors on the space-time grid. When a new cluster is born we record its D^2_{min} value as its birth. Birth values are only achieved when the maxima is not adjacent to any existing clusters. When two existing clusters merge, we record their D^2_{min} value as their death. No additional cluster is created after merging. Surviving clusters die when reaching the lowest D^2_{min} value. We can then place each cluster in a birth-death diagram [Fig. 1(b)] and compute their persistence p as the distance of the cluster to the line $y(\text{death}) = x(\text{birth})$. Events that correspond to short space-time fluctuations will be close to this line. When looking at

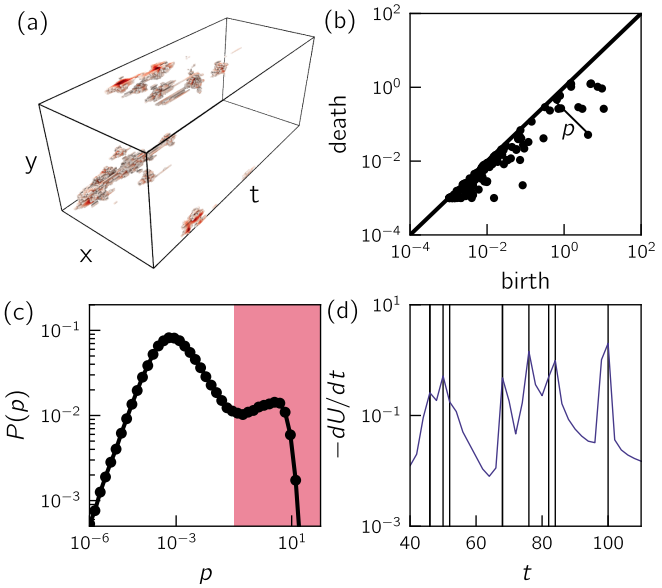

FIG. 1. Persistent homology clustering. (a) Space-time map of the plastic activity monitored by the $D^2_{\min}$ field for a typical avalanche in a glass with $N = 160 \times 160$. (b) Birth-death phase diagram of individual local maxima of our $D^2_{\min}$ grid. The persistent p of a given event is given as the distance to the line $y(\text{death}) = x(\text{birth})$. (c) Probability distribution of the persistent averaged over an ensemble of avalanches. The red area indicates our threshold $p > 0.1$ for persistent events. (d) Superposition of the actual dissipation $-dU/dt$ and birth time of individual events with $p > 0.1$.

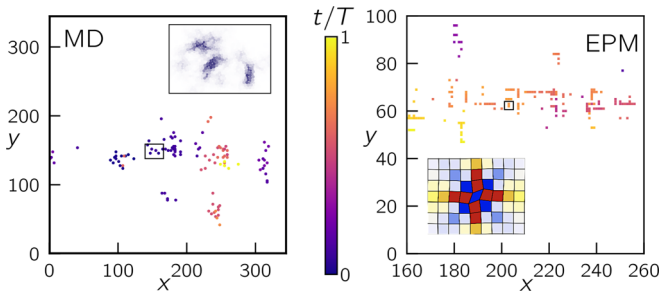

FIG. 2. Spatiotemporal plastic evolution. Typical spatiotemporal map of an avalanche in molecular dynamics (MD) with gradient descent dynamics (left) and in the elastoplastic model (EPM) with synchronous dynamics (right). Each plastic event is colored according to its normalized birth time t/T, with T the avalanche duration. Insets show the particle resolved plastic field (left) and EPM local stress redistribution (right). System sizes are $L = 320$ and $L = 256$ for MD and EPM, respectively. For visibility only a subset of the system is shown for the EPM.

the probability distribution of persistence $P(p)$ averaged over many avalanches [Fig. 1(c)], we observe a bimodal distribution that indicates two different populations of individual events. Selecting events that have a large persistence $p > 0.1$ and superimposing their birth time on the avalanche activity time profile (energy dissipation $-dU/dt$), we find that the identified persistent clusters perfectly match the time location of large dissipation [Fig. 1(d)]. For each persistent cluster, we have access to its spatial position in addition to its birth time. This allows us to construct the same spatiotemporal map of plastic activity as in our EPM, with individual events occurring at "sites" corresponding to these persistent peaks.

C. Mesoscale model

For the EPM, we use the same shear transformation based model in [39] with the same initialization and evolution rules but with different loading—forward shearing instead of cyclic. The dynamical update rules under an applied global shear strain are (i) for a given stress field, synchronously allow all sites over threshold to yield and recompute the stress field everywhere; (ii) repeat (i) until all sites are below threshold; and (iii) advance the globally applied total strain until precisely one site is at its stability threshold. The synchronous update of unstable sites defined in step (i) sets the time unit of the model.

In our elastoplastic model [39], the two-dimensional (2D) plane is discretized into sites. Each site has an elastic strain ϵ_e and a plastic strain ϵ_p, with the total strain defined as the sum of the two: $\epsilon_t = \epsilon_e + \epsilon_p$. The stress σ is proportional to $\epsilon_e : \sigma = 2\mu\epsilon_e$, where σ is defined in terms of the Cartesian components of the stress: $\sigma = (\sigma_{xx} - \sigma_{yy})/2$, and similarly, $\epsilon_e = (\epsilon_e^{xx} - \epsilon_e^{yy})/2$. We set $\mu = 1$ throughout this study, so σ and ϵ_e are numerically equal. When the magnitude of the stress at a site exceeds the plastic threshold, set to 1 here, we increment the plastic strain at the site in the same direction as σ (+2 for $\sigma \geqslant 1$, –2 for $\sigma \leqslant -1$) and update the stress at the remaining sites according to the rules of linear elasticity analogous to Eshelby's classical solution for a plastic inclusion in an elastic matrix. Throughout this paper, we use the terms "yield stress" and "threshold" interchangeably. The increment value 2 is chosen to ensure a single-valued strain energy function. The total number of avalanches collected is 90k, obtained from shearing 50 different systems ($L = 256$). The avalanche size S is defined as the total stress drop which is proportional to the total number of plastic transformations. The duration T is defined as the total number of sweeps in the avalanche. As time in the EPM is discrete and defined by the number of sweeps accumulated during the course of the event, the energy dissipation rate is simply defined as the total energy drop in a given sweep.

III. RESULTS

A. Spatiotemporal plastic evolution

We first qualitatively describe a typical avalanche in both models. Figure 2 highlights individual sites that have yielded, colored according to the time at which the site toppled. The pattern which emerges is a set of clusters where all sites within a cluster are nearly the same color, extend along a direction of maximum shear, and almost continuously fill space; additional MD avalanches are shown in the SM [36].

In contrast, these larger clusters are typically separated from one another by gaps of material. Nearby clusters are not necessarily triggered sequentially in time, suggesting that gaps between clusters correspond to regions of material that are stable enough to survive the increased local stresses at the edges of the growing cluster. The same intermittent activity

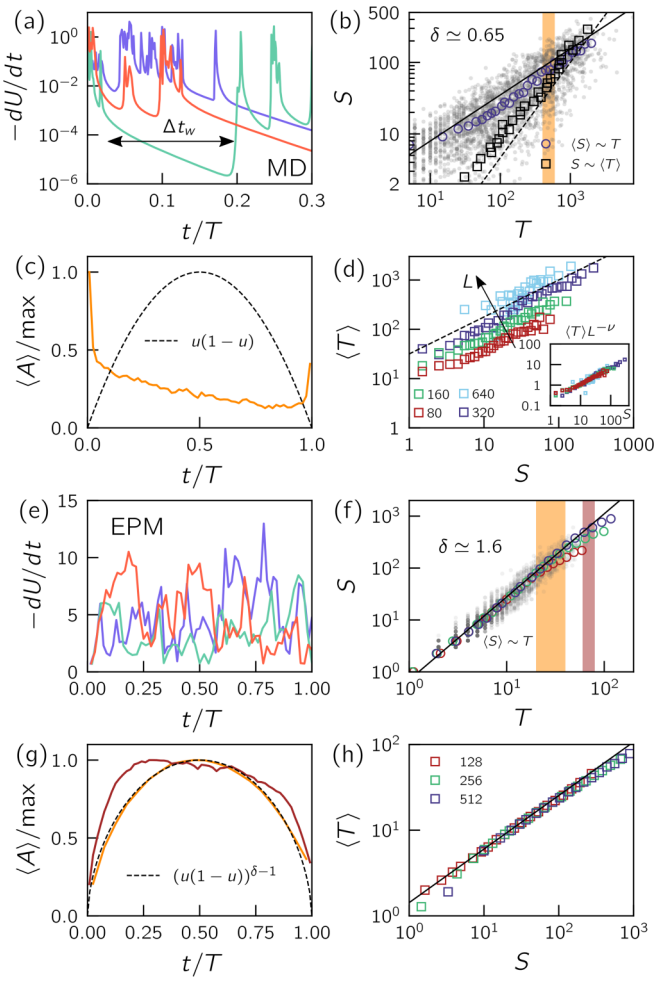

FIG. 3. Plastic activity profile. (a) Typical dissipation rate $-dU/dt$ in MD plotted as a function of the reduced time t/T for duration $1500 < T < 3000$ and $L = 320$. (b) Scatter plot of avalanche size vs duration. The blue and black empty symbols are running means $\langle S\rangle \sim T$ and $\langle T\rangle \sim S$, respectively. Solid and dashed lines indicate the scaling $\langle S\rangle \sim T^{\delta}$, with exponent $\delta = 0.65$ and $\delta = 4/3$, respectively. (c) Average normalized activity for $400 < T < 600$ [orange region in (b)]. (d) Average duration $\langle T\rangle$ at a fixed avalanche size S for different system sizes. Insets show the same data collapsed using $\langle T\rangle L^{-\nu}$, with $\nu \simeq 0.8$. Panels (e), (f), (g), and (h) show the same results as in (a), (b), (c), and (d) but for the EPM where $-dU/dt$ is measured as the energy dissipation per sweep and $L = 256$.

is found in depinning avalanches with long-range interactions [40,41].

B. Plastic activity profile

Given this qualitative similarity in the spatiotemporal structure and the utility of mean-field models in predicting temporal dynamics in depinning and other disordered critical phenomena, we next quantitatively analyze the temporal activity profiles in MD and EPM. In Figs. 3(a) and 3(e), we plot the dissipation rate $-dU/dt$ as a function of the normalized duration t/T for a few typical avalanches. In MD we find intermittent bursts of activity followed by long quiescent periods, so that the energy dissipation magnitude spans six decades. Waiting times are associated with marginally unstable sites with $\Delta\sigma_+ = \sigma_i - \sigma_i^{\text{th}} > 0$, with σ_i and σ_i^{th} the local stress and local yield stress of the unstable site i. For a typical saddle-node bifurcation, we expect that the waiting time Δt_w before departure will scale as $\Delta t_w \sim \Delta\sigma_+^{-1/2}$ [42]. In contrast, unstable sites in our EPM transform instantaneously regardless of how far they are over threshold, termed a uniform activation rate. As a consequence, activity fluctuations in EPM [Fig. 3(e)] vary by less than an order of magnitude.

Another difference between the MD and EPM can be seen by plotting the avalanche size S versus duration T, Figs. 3(b) for MD and 3(f) for EPM. We find that MD data scatter much more than our EPM. This is similar to previous results comparing an EPM with a uniform activation rate to one with a so-called progressive rate model, where the activation rate is a function of the overshoot $\sigma_i - \sigma_i^{\text{th}}$ [32,43]. In both MD and EPM, the average size for a fixed duration shows a power law $\langle S\rangle \propto T^{\delta}$, where the dynamical exponent $\delta = d_f/z$, with d_f and z the static and dynamical fractal exponent, respectively. Independent estimation of d_f and z are reported in the Supplemental Material [36] and are consistent with previous works [11,13]. The EPM gives a larger δ than MD, as the dynamical exponent $z \simeq 0.6$ is lower than MD ($z \simeq 1.55$), although it is consistent with previous EPM-type models [11] which used continuous-in-time dynamics rather than the automaton rules we apply here.

More surprisingly, in MD we find a discrepancy between average avalanche size for a fixed duration $\langle S\rangle_T$ and the average duration for a fixed size $\langle T\rangle_S$. We find that the average duration $\langle T\rangle_S$ is system-size dependent and grows with L as L^{ν}, see Fig. 3(d). We can understand this size effect as follows. During avalanches the system visits configurations with *unstable* sites with $\Delta\sigma_+ > 0$. We expect the average stability of the least *unstable* site to decrease with system size as $\langle \Delta\sigma_+\rangle \sim L^{-\eta}$. This scaling of the characteristic overshoot for unstable sites is different from the previously reported scaling for thresholds associated with marginally *stable* sites [26,44–46]. In our EPM model, the marginally *unstable* sites immediately yield and generate new stress fields. The situation is different in our MD under gradient descent dynamics. As discussed above, a waiting time Δt_w associated with the departure from a saddle node emerges. The average waiting time caused by this marginal triggering will thus be size dependent and follow $\langle \Delta t_w\rangle \sim L^{\nu}$. We find a good collapse of MD data for $\nu \simeq 0.8$. A similar finite-size effect, though with a different exponent, was previously noticed in progressive rate EPMs [32,43].

In Figs. 3(c) and 3(g), we show the normalized average activity profile $\langle A\rangle/\langle A\rangle_{\max}$ (with $A = -dU/dt$) plotted against the reduced time t/T in the MD and EPM, respectively. For the EPM and avalanches within the scaling regime, we find that profiles are symmetrical and well modelled by $f(u) = [u(1-u)]^{\delta-1}$, with $u = t/T$, consistent with previous works and mean-field theories [11,47]. For large avalanches in EPM, with long duration beyond the scaling regime where system-size effects become relevant, one finds a profile which departs from that scaling and is skewed with more activity at early times. A similar transition to skewed profiles for large evens was recently observed in granular flows [48]. In MD

the profile deviates strongly from the $f(u) = [u(1-u)]^{\delta-1}$ form. This is due to inactive periods with almost zero dissipation. The average activity at the midpoint of the avalanche is systematically lower than at its beginning, the latter being by definition always active. We speculate that one would recover a symmetrical activity profile by introducing inertia in the dynamics, which would facilitate barrier crossing in weakly unstable regions.

C. Spatiotemporal plastic correlation

We next analyze the spatial correlations that build up during the avalanche. To do this we define a two-points two-times correlation function $C(\vec{r}_0, \vec{r}_0 + \vec{r}, t_0, t_0 + \Delta t) = \langle \overline{\Delta P(\vec{r}_0, t_0) \Delta P(\vec{r}_0 + \vec{r}, t_0 + \Delta t)} \rangle$, with $\Delta P = P - \overline{P}$ and where $\overline{...}$ and $\langle ... \rangle$ represent a spatial and ensemble average, respectively. Here, $P(\vec{r}, t)$ corresponds to the incremental plastic field measured at a given time t. For both MD and EPM avalanches, $P(\vec{r}, t)$ corresponds to a binary field of 0 and 1 for inactive or active sites, respectively.

Figure 4(a) shows the MD normalized correlation $C(x, y)/C_{\max}$ for delay times $\Delta t = 4$ (left) and 40 (right). There are positive correlations along the directions of imposed shear (the x and y axes). The spatial extent of the region of positive correlation grows with Δt [49]. The same data are shown for the EPM in Fig. 4(e) for $\Delta t = 2$ and 6, where we observe the same qualitative behavior.

In Figs. 4(b) and 4(f) we plot $C(x)$ along the x axis at various Δt. $C(x)$ decays exponentially at small x, and we use the exponential decay rate to define a short-range length scale ξ_{excite}. In practice, fits only include data with $C(x)/C_{\max} > 0.05$. Despite the initial exponential decay, $C(x)$ stops behaving exponentially and crosses through zero at a finite x, which corresponds to the length scale at which the plasticity starts to become anticorrelated, see Figs. 4(c) and 4(g). We use this zero crossing to define a second, larger length scale, ξ_{marginal}. Note that for large system sizes and large Δt where our statistics are poor, several negative crossings can occur. In such a case we evaluate an estimate of the error on ξ_{marginal} as the spread between the first negative crossing and the median over all negative crossings. Importantly, we observe that ξ_{marginal} is size dependent and grow with L. We also look at correlation in the transverse direction, $C(y)$ at a small, fixed x ($x_{\text{MD}} = 50$ and $x_{\text{EPM}} = 40$). Results are shown for various Δt in Figs. 4(d) and 4(h). We find that $C(y)$ is well modeled by a Gaussian, $C(y) \sim e^{-(y/w)^2/2}$, which allows us to quantify the width w associated with plastic propagation.

In order to improve the statistics of the particle-based correlations, we assume time-translational invariance and average over t_0. Data examining the validity of this assumption is shown for both MD and EPM in Figs. 5(a) and 5(b). Here we plot the correlation along the principal shear axis (x axis) and check to what extent $C(t_0 = 0, x) = C(t_0 > 0, x)$ is valid. We find that time translation invariance holds relatively well in the early decay. We find a slightly larger likelihood to find more plasticity further in space for $t_0 > 0$ than for $t_0 = 0$. This trend can be explained by the progressive accumulation of stress redistribution across the system, which makes it more likely for marginal sites with $\Delta\sigma_- < 0$ to yield away from the original source. We fix $t_0 = 0$ to extract the negative crossing below in Fig. 6, but we average over t_0 to study the initial decay of $C(x)$.

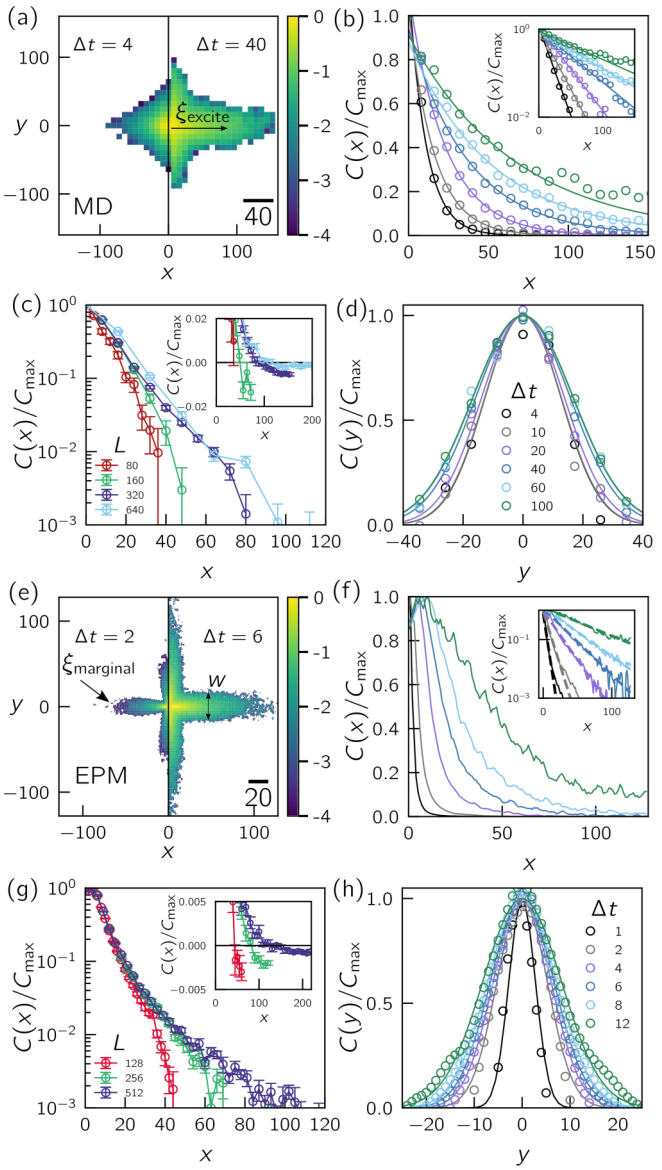

FIG. 4. Spatiotemporal plastic propagation. (a) Particle-based (MD) two-points two-times normalized correlation function $C(x, y)/C_{\max}$ in $\log_{10}$ for $\Delta t = 4$ and 40. White regions correspond to a negative correlation. The system size is $L = 320$. (b) Correlation function along the main stress redistribution for different delay times $\Delta t = 4$, 10, 20, 40, 60, and 100. Inset shows the correlation in semilog scale. Solid lines are fits of the form $C(x)/C_{\max} \sim e^{-x/\xi_{\text{excite}}}$, with ξ_{excite} a short-length-scale decay. (c) Change of $C(x)/C_{\max}$ for different system size at a fixed $\Delta t = 6$. Inset shows the negative crossing in linear scale. (d) Transverse normalized correlation function $C(y)/C_{\max}$ at a fixed $x_{\text{MD}} = 50$ for different Δt. Solid lines are fits with $C(y) \sim e^{-(y/w)^2/2}$, where w is the width of the plastic localization. (e), (f), (g), and (h) The same results as in (a), (b), (c), and (d) but for our mesoscale model (EPM) with $\Delta t = 1$, 2, 4, 6, 8, and 12 and $L = 256$. $C(x)/C_{\max}$ in (g) is for $\Delta t = 3$. $C(y)/C_{\max}$ in (h) is evaluated at $x_{\text{EPM}} = 40$. The meanings of ξ_{excite}, ξ_{marginal}, and w are illustrated in (a) and (e).

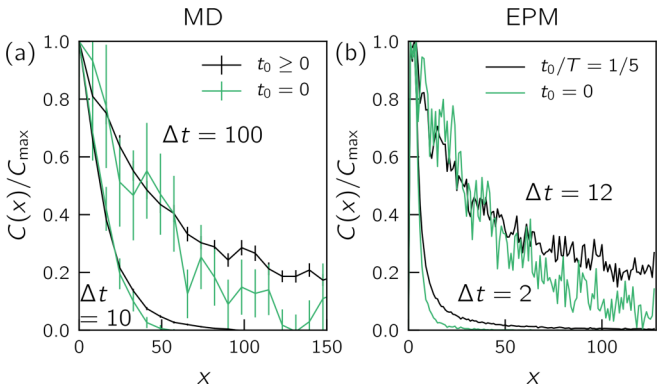

FIG. 5. Time translational invariance. (a) Comparison of the MD incremental correlation $C = \overline{\langle \Delta f(\vec{r}_0, t_0) \Delta f(\vec{r}_0 + \vec{r}, t_0 + \Delta t) \rangle}$ for $t_0 = 0$ (green) and $t_0 \geqslant 0$ (black). (b) Same data as in (a) for our EPM but with $t_0 = 0$ (green) and $t_0/T = 1/5$ (black). System sizes are $L = 320$ and $L = 256$ for MD and EPM, respectively.

D. Spatiotemporal plastic propagation

We now discuss how the short correlation decay ξ_{excite}, the long-range marginal length ξ_{marginal}, and the plastic width w vary with Δt as well as with the system size L. We remind the reader that the length associated with an EPM site corresponds

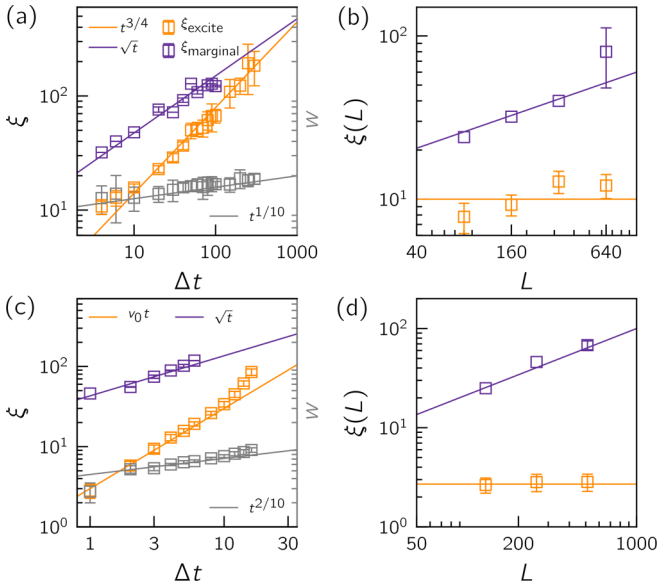

FIG. 6. Plastic length scales. (a) MD data for ξ_{excite} (orange) and ξ_{marginal} (purple) plotted against Δt with $L = 320$. The purple line corresponds to the diffusive response associated with the stress field generated by a single event at $\Delta t = 0$. The orange line indicates a superdiffusive regime with $\sim t^{3/4}$. Gray data are the plastic width w extracted from fitting $C(y)$. The gray line indicates a subdiffusive regime with $\sim t^{1/10}$. (b) ξ_{excite} and ξ_{marginal} for $\Delta t = t_{\text{STZ}} = 6$ plotted as a function of the system size L. $\xi_{\text{marginal}}(L)$ scales as $\sim L^{1/3}$. (c) and (d) are the same results as in (a), (b), but for our mesoscale model (EPM) with $L = 256$. The solid orange line in (g) indicates $v_0 t$, with $v_0 = 3$. Results in (d) are for $\Delta t = 1$, where $\xi_{\text{marginal}}(L)$ scales as $\sim L^{2/3}$. $\xi_{\text{excite}}(L)$ is fairly constant for both MD and EPM. The mean and error bar for ξ_{marginal} are estimated as the arithmetic mean and the spread between the first negative crossing and the median over all negative crossings (if any), respectively.

to a few particle diameters in MD. In Figs. 6(a) and 6(c) we show that these three lengths exhibit a power-law evolution with Δt. The trends are similar in both MD and EPM. ξ_{excite} has the strongest Δt dependence: it scales like $\Delta t^{3/4}$ in the MD and is nearly ballistic in the EPM. ξ_{marginal} scales diffusively as $\Delta t^{1/2}$ in both the MD and EPM. w has a very weak dependence on Δt, which indicates that for any given avalanche, the correlations get more and more constrained to lie along the axes of shear as time goes during the course of the avalanche. We speculate that the weak growth in time of plastic width is due to the negative interference of the stress redistribution that promotes unidirectional plastic propagation. Finally, in Figs. 6(b) and 6(d) we show how ξ_{marginal} and ξ_{excite} depend on system size for a fixed, small Δt. In both MD and EPM, ξ_{excite} has relatively little dependence on system size, while ξ_{marginal} has a more pronounced system-size dependence, scaling approximately like $L^{1/3}$ and $L^{2/3}$ in the MD and EPM, respectively. The present size effect can be explained by the presence of marginally *stable* sites with $\Delta\sigma_- = \sigma_i - \sigma_i^{\text{th}} < 0$ (to be contrasted with the marginally *unstable* sites discussed above) and the long-range nature of the stress generated from the initial source. We know from previous works that $\langle \Delta\sigma_- \rangle \sim L^{-1.21}$ [46] and $\langle \Delta\sigma_- \rangle \sim L^{-1.35}$ [26] for MD and EPM, respectively. Moreover, the Eshelby stress kernel decays as $\sim r^{-d}$. Thus we expect a characteristic scale ξ_{marginal} to emerge where the Eshelby kernel will decay to the level of $\Delta\sigma_-$ for a given system size. Beyond that length scale no marginal triggering will be possible. From the scaling of $\Delta\sigma_-$, we expect $\xi_{\text{marginal}} \sim L^{0.6}$ (for MD) and $\xi_{\text{marginal}} \sim L^{0.725}$ (for EPM). Our data for ξ_{marginal} show less sensitive system-size dependence than that for both the MD and EPM.

IV. DISCUSSION AND OUTLOOK

In this paper we demonstrate that the spatiotemporal evolution of avalanches in particle-based simulations in the overdamped limit share important similarities and differences with an elastoplastic model governed by synchronous dynamics. We show that in both models avalanches are driven by localized clusters of activity and that the spatial correlation function of activity remains largely confined to a strip which does not appreciably widen in time and exhibits two length scales that grow differently in time and with system size.

One length scale, ξ_{excite}, corresponds to high-likelihood nearby events which are mechanically excited. In the EPM models this leads to standard ballistic propagation as seen in other excitable media [27], while in MD simulations we find the front propagates as $t^{3/4}$. In both cases our data suggests this scale is independent of system size. An interesting question for future work is what generates this nonstandard exponent in MD simulations.

A second, longer length scale, ξ_{marginal}, corresponding to low-likelihood remote events, propagates diffusively and scales with system size. This suggests that it is governed by the weakest spots in the disordered solid, as far-field stress fluctuations anywhere in the system are sufficient to trigger events, and the stress magnitude required to trigger the weakest spot scales as a power law with system size. Given the low probability of these marginally triggered events, it is

statistically more demanding to quantify ξ_{marginal} than ξ_{excite}. Although it is comforting that the size dependence we measure for ξ_{marginal} is consistent with the known size scaling of the weakest site [26,32,45,46], we nevertheless admit that the dynamics is dominated by the excited toppling mechanism [27] and that ξ_{marginal} may be less important for the avalanche evolution.

Another difference between the two types of simulations is the statistics of their temporal dynamics. In MD simulations the stress overshoot—the difference between the triggering stress field and the stress threshold of an excitable site–governs how fast the system departs a saddle and the waiting times between localized bursts of deformation in an avalanche. These effects generate dynamical exponents that depart significantly with mean-field predictions and cause duration-size curves to vary with system size. In contrast, our simple EPM has no such mechanism; the dynamical exponent is much closer to mean field, and the duration-size curves do not depend on system size. Recent progressive-rate EP models [32,43] include a proxy for this waiting time and qualitatively reproduce this physics but do not quantitatively match the exponents we find in the MD. A nice feature of EPMs is that it is possible to disambiguate the consequences of various choices for the stress propagation, waiting times, and disorder. Future work could focus on adjusting properties of EPMs to improve quantitative agreement with MD. Another important avenue is understanding how these models behave in the presence of inertia [9,25,50]. In practice, one will have to introduce in EPM realistic stress propagation such as proposed in Refs. [51,52] using finite element methods.

We speculate that our results should translate well to three-dimensional (3D) solids. In particular, the long-range elastic kernel will give rise to the "domino effect" and the corresponding fast growth in time of ξ_{excite}. Moreover, as the statistics of marginally stable sites have been shown to follow a similar scaling as found in 2D, we also expect a size-dependent ξ_{marginal}.

We have focused here on MD and EPM simulations for a relatively ductile material, where the stress required for each site to be triggered is relatively small. It will be very interesting to revisit similarities and differences in brittle systems that undergo shear banding instabilities, which provide an even stricter test of models of the spatiotemporal evolution of disordered solids. More broadly, the tools developed here could be used to characterize spatiotemporal dynamics of avalanches in materials with complicated interactions (irregular shapes, friction, realistic molecular potentials) and boundary conditions.

ACKNOWLEDGMENTS

We acknowledge support of the Simons Foundation for "Cracking the Glass Problem Collaboration" Awards No. 348126 (D.R.) and No. 454947 (A.E. and M.L.M.). M.L.M. acknowledges support from NSF-DMR-1951921. D.R. acknowledges support by the H2020-MSCA-IF-2020 project ToughMG (No. 101024057).

[1] G. Durin and S. Zapperi, Scaling Exponents for Barkhausen Avalanches in Polycrystalline and Amorphous Ferromagnets, Phys. Rev. Lett. **84**, 4705 (2000).

[2] F. Dalton and D. Corcoran, Self-organized criticality in a sheared granular stick-slip system, Phys. Rev. E **63**, 061312 (2001).

[3] K. J. Måløy, S. Santucci, J. Schmittbuhl, and R. Toussaint, Local Waiting Time Fluctuations along a Randomly Pinned Crack Front, Phys. Rev. Lett. **96**, 045501 (2006).

[4] J. P. Sethna, K. A. Dahmen, and C. R. Myers, Crackling noise, Nature (London) **410**, 242 (2001).

[5] B. A. Sun, H. B. Yu, W. Jiao, H. Y. Bai, D. Q. Zhao, and W. H. Wang, Plasticity of Ductile Metallic Glasses: A Self-Organized Critical State, Phys. Rev. Lett. **105**, 035501 (2010).

[6] J. Lin, T. Gueudré, A. Rosso, and M. Wyart, Criticality in the Approach to Failure in Amorphous Solids, Phys. Rev. Lett. **115**, 168001 (2015).

[7] Z. Budrikis, D. F. Castellanos, S. Sandfeld, M. Zaiser, and S. Zapperi, Universal features of amorphous plasticity, Nat. Commun. **8**, 15928 (2017).

[8] M. Talamali, V. Petäjä, D. Vandembroucq, and S. Roux, Avalanches, precursors and finite size fluctuations in a mesoscopic model of amorphous plasticity, Phys. Rev. E **84**, 016115 (2011).

[9] K. M. Salerno, C. E. Maloney, and M. O. Robbins, Avalanches in Strained Amorphous Solids: Does Inertia Destroy Critical Behavior? Phys. Rev. Lett. **109**, 105703 (2012).

[10] J. Lin, E. Lerner, A. Rosso, and M. Wyart, Scaling description of the yielding transition in soft amorphous solids at zero temperature, Proc. Natl. Acad. Sci. USA **111**, 14382 (2014).

[11] C. Liu, E. E. Ferrero, F. Puosi, J.-L. Barrat, and K. Martens, Driving Rate Dependence of Avalanche Statistics and Shapes at the Yielding Transition, Phys. Rev. Lett. **116**, 065501 (2016).

[12] J. T. Clemmer, K. M. Salerno, and M. O. Robbins, Criticality in sheared, disordered solids, I. Rate effects in stress and diffusion, Phys. Rev. E **103**, 042605 (2021).

[13] J. T. Clemmer, K. M. Salerno, and M. O. Robbins, Criticality in sheared, disordered solids, II. Correlations in avalanche dynamics, Phys. Rev. E **103**, 042606 (2021).

[14] C. E. Maloney and M. O. Robbins, Anisotropic Power Law Strain Correlations in Sheared Amorphous 2D Solids, Phys. Rev. Lett. **102**, 225502 (2009).

[15] M. Talamali, V. Petäjä, D. Vandembroucq, and S. Roux, Strain localization and anisotropic correlations in a mesoscopic model of amorphous plasticity, C. R. Mec. **340**, 275 (2012).

[16] J. Chattoraj and A. Lemaître, Elastic Signature of Flow Events in Supercooled Liquids Under Shear, Phys. Rev. Lett. **111**, 066001 (2013).

[17] A. Nicolas, J. Rottler, and J.-L. Barrat, Spatiotemporal correlations between plastic events in the shear flow of athermal amorphous solids, Eur. Phys. J. E **37**, 50 (2014).

[18] F. Puosi, J. Rottler, and J.-L. Barrat, Plastic response and correlations in athermally sheared amorphous solids, Phys. Rev. E **94**, 032604 (2016).

[19] J. Antonaglia, W. J. Wright, X. Gu, R. R. Byer, T. C. Hufnagel, M. LeBlanc, J. T. Uhl, and K. A. Dahmen, Bulk Metallic Glasses Deform via Slip Avalanches, Phys. Rev. Lett. **112**, 155501 (2014).

[20] A. Nicolas, E. E. Ferrero, K. Martens, and J.-L. Barrat, Deformation and flow of amorphous solids: Insights from elastoplastic models, Rev. Mod. Phys. **90**, 045006 (2018).

[21] J.-C. Baret, D. Vandembroucq, and S. Roux, An Extremal Model of Amorphous Plasticity, Phys. Rev. Lett. **89**, 195506 (2002).

[22] Z. Budrikis and S. Zapperi, Avalanche localization and crossover scaling in amorphous plasticity, Phys. Rev. E **88**, 062403 (2013).

[23] B. Tyukodi, D. Vandembroucq, and C. E. Maloney, Diffusion in Mesoscopic Lattice Models of Amorphous Plasticity, Phys. Rev. Lett. **121**, 145501 (2018).

[24] F. Puosi, J. Rottler, and J.-L. Barrat, Time-dependent elastic response to a local shear transformation in amorphous solids, Phys. Rev. E **89**, 042302 (2014).

[25] K. M. Salerno and M. O. Robbins, Effect of inertia on sheared disordered solids: Critical scaling of avalanches in two and three dimensions, Phys. Rev. E **88**, 062206 (2013).

[26] B. Tyukodi, D. Vandembroucq, and C. E. Maloney, Avalanches, thresholds, and diffusion in mesoscale amorphous plasticity, Phys. Rev. E **100**, 043003 (2019).

[27] T. Idema and A. J. Liu, Mechanical signaling via nonlinear wavefront propagation in a mechanically excitable medium, Phys. Rev. E **89**, 062709 (2014).

[28] P. Sollich, F. Lequeux, P. Hébraud, and M. E. Cates, Rheology of Soft Glassy Materials, Phys. Rev. Lett. **78**, 2020 (1997).

[29] A. Lemaître and C. Caroli, Plastic response of a two-dimensional amorphous solid to quasistatic shear: Transverse particle diffusion and phenomenology of dissipative events, Phys. Rev. E **76**, 036104 (2007).

[30] E. Agoritsas, E. Bertin, K. Martens, and J.-L. Barrat, On the relevance of disorder in athermal amorphous materials under shear, Eur. Phys. J. E **38**, 71 (2015).

[31] J. Lin and M. Wyart, Mean-Field Description of Plastic Flow in Amorphous Solids, Phys. Rev. X **6**, 011005 (2016).

[32] E. E. Ferrero and E. A. Jagla, Criticality in elastoplastic models of amorphous solids with stress-dependent yielding rates, Soft Matter **15**, 9041 (2019).

[33] E. Lerner, Mechanical properties of simple computer glasses, J. Non-Cryst. Solids **522**, 119570 (2019).

[34] M. Ozawa, L. Berthier, G. Biroli, A. Rosso, and G. Tarjus, Random critical point separates brittle and ductile yielding transitions in amorphous materials, Proc. Natl. Acad. Sci. USA **115**, 6656 (2018).

[35] D. Richard, M. Ozawa, S. Patinet, E. Stanifer, B. Shang, S. A. Ridout, B. Xu, G. Zhang, P. K. Morse, J.-L. Barrat, L. Berthier, M. L. Falk, P. Guan, A. J. Liu, K. Martens, S. Sastry, D. Vandembroucq, E. Lerner, and M. L. Manning, Predicting plasticity in disordered solids from structural indicators, Phys. Rev. Mater. **4**, 113609 (2020).

[36] See Supplemental Material at http://link.aps.org/supplemental/10.1103/PhysRevE.107.034902 for technical details about the simulations, along with some additional supporting results.

[37] M. L. Falk and J. S. Langer, Dynamics of viscoplastic deformation in amorphous solids, Phys. Rev. E **57**, 7192 (1998).

[38] E. Stanifer and M. L. Manning, Avalanche dynamics in sheared athermal particle packings occurs via localized bursts predicted by unstable linear response, Soft Matter **18**, 2394 (2022).

[39] K. Khirallah, B. Tyukodi, D. Vandembroucq, and C. E. Maloney, Yielding in an Integer Automaton Model for Amorphous Solids under Cyclic Shear, Phys. Rev. Lett. **126**, 218005 (2021).

[40] L. Laurson, S. Santucci, and S. Zapperi, Avalanches and clusters in planar crack front propagation, Phys. Rev. E **81**, 046116 (2010).

[41] C. Le Priol, P. Le Doussal, and A. Rosso, Spatial Clustering of Depinning Avalanches in Presence of Long-Range Interactions, Phys. Rev. Lett. **126**, 025702 (2021).

[42] S. H. Strogatz, *Nonlinear Dynamics and Chaos with Student Solutions Manual: With Applications to Physics, Biology, Chemistry, and Engineering* (CRC Press, Boaca Raton, FL, 2018).

[43] I. Fernandez Aguirre and E. A. Jagla, Critical exponents of the yielding transition of amorphous solids, Phys. Rev. E **98**, 013002 (2018).

[44] S. Karmakar, E. Lerner, and I. Procaccia, Statistical physics of the yielding transition in amorphous solids, Phys. Rev. E **82**, 055103(R) (2010).

[45] J. Lin, A. Saade, E. Lerner, A. Rosso, and M. Wyart, On the density of shear transformations in amorphous solids, Europhys. Lett. **105**, 26003 (2014).

[46] C. Ruscher and J. Rottler, Residual stress distributions in amorphous solids from atomistic simulations, Soft Matter **16**, 8940 (2020).

[47] L. Laurson, X. Illa, S. Santucci, K. T. Tallakstad, K. J. Måløy, and M. J. Alava, Evolution of the average avalanche shape with the universality class, Nat. Commun. **4**, 2927 (2013).

[48] A. Baldassarri, M. Annunziata, A. Gnoli, G. Pontuale, and A. Petri, Breakdown of scaling and friction weakening in intermittent granular flow, Sci. Rep. **9**, 16962 (2019).

[49] Note that small deviations from an ideal $x \leftrightarrow y$ symmetry stem from the use of Lees-Edwards periodic boundary conditions.

[50] K. Karimi, E. E. Ferrero, and J.-L. Barrat, Inertia and universality of avalanche statistics: The case of slowly deformed amorphous solids, Phys. Rev. E **95**, 013003 (2017).

[51] A. Nicolas, F. Puosi, H. Mizuno, and J.-L. Barrat, Elastic consequences of a single plastic event: Towards a realistic account of structural disorder and shear wave propagation in models of flowing amorphous solids, J. Mech. Phys. Solids **78**, 333 (2015).

[52] K. Karimi and J.-L. Barrat, Role of inertia in the rheology of amorphous systems: A finite-element-based elastoplastic model, Phys. Rev. E **93**, 022904 (2016).